Unveiling the anisotropic fractal magnetic domain structure in bulk crystals of antiskyrmion host $(Fe,Ni,Pd)_3P$ by small-angle neutron scattering[1]

Kosuke Karube,[a]* Victor Ukleev,[b] Fumitaka Kagawa,[a,c] Yoshinori Tokura,[a,c,d] Yasujiro Taguchi[a]* and Jonathan S. White[b]*

[a]RIKEN Center for Emergent Matter Science (CEMS), Wako, 351-0198, Japan, [b]Laboratory for Neutron Scattering and Imaging, Paul Scherrer Institute, Villigen, CH-5232, Switzerland, [c]Department of Applied Physics, University of Tokyo, Bunkyo-ku, 113-8656, Japan, and [d]Tokyo College, University of Tokyo, Bunkyo-ku, 113-8656, Japan. *Correspondence e-mail: kosuke.karube@riken.jp, y-taguchi@riken.jp, jonathan.white@psi.ch

Intermetallic Pd-doped $(Fe,Ni)_3P$, which crystallizes in a non-centrosymmetric tetragonal structure with S_4 symmetry, has recently been discovered to host magnetic antiskyrmions, antivortex-like topological spin textures. In this material, uniaxial magnetic anisotropy and dipolar interactions play a significant role, giving rise to finely branched magnetic domain patterns near the surface of bulk crystals, as revealed by a previous magnetic force microscopy (MFM) measurement. However, small-angle neutron scattering (SANS) is a more suitable method for characterizing bulk properties and fractal structures on the mesoscopic length scale. In this study, using SANS and MFM, the magnetic domain structure in bulk single crystals of $(Fe_{0.63}Ni_{0.30}Pd_{0.07})_3P$ is quantitatively investigated. The SANS results demonstrate that the magnetic domain structure exhibits anisotropic fractal character on length scales down to the width of the magnetic domain walls. The fractal features are gradually lost in magnetic fields, and different field dependencies are observed at 300 and 2 K due to a temperature-dependent anisotropy. This study quantifies the fractality of the highly anisotropic magnetic domain structures in an antiskyrmion material, and highlights the versatility of SANS for the study of fractal structures in magnetic systems.

1. Introduction

Small-angle neutron scattering (SANS) is a powerful tool for determining magnetic structures in condensed matter physics (Mühlbauer *et al.*, 2019). SANS provides unique information for characterizing bulk properties over the mesoscopic length scale from a few nanometres to several hundred nanometres. This is a very important length regime in which various types of magnetic structures emerge. Magnetic domains (Malozemoff & Slonczewski, 1979; Hubert & Schäfer, 1998) and magnetic skyrmions (Mühlbauer *et al.*, 2009; Yu *et al.*, 2010; Nagaosa & Tokura, 2013) are typical examples of such mesoscopic magnetic structures. Skyrmions are vortex-like spin textures characterized by an integer topological charge. They have been extensively studied in the past decade in various magnetic systems as a source of emergent electromagnetic phenomena, and with an anticipation of potential applications in spintronics devices (Tokura & Kanazawa, 2021).

Recently, a new antivortex-like topological spin texture – the antiskyrmion, in which the sign of the topological charge is opposite to that of the skyrmion – has attracted much attention. Antiskyrmions are topologically distinct from conventional (type I and II) bubble domains and skyrmions and are
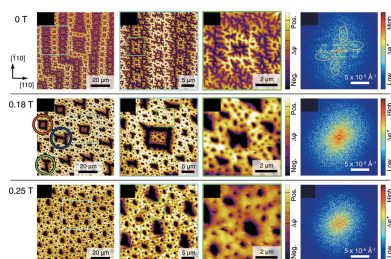
composed of both Bloch and Néel walls with reversed helicities along two orthogonal axes, *i.e.* with fourfold roto-inversion ($\bar{4}$) symmetry. This unique magnetic texture originates from the anisotropic Dzyaloshinskii–Moriya interaction (DMI) in the non-centrosymmetric crystal structure belonging to D_{2d} or S_4 symmetry (Bogdanov & Yablonskii, 1989; Leonov *et al.*, 2016). In contrast to a number of skyrmion materials, antiskyrmions have thus far been observed only in thin plates (100–200 nm thickness) of Heusler alloys with D_{2d} symmetry, *e.g.* $Mn_{1.4}PtSn$ (Nayak *et al.*, 2017; Peng *et al.*, 2020), and Pd-doped schreibersite $(Fe,Ni)_3P$ with S_4 symmetry, *i.e.* $(Fe_{0.63}Ni_{0.30}Pd_{0.07})_3P$ (Karube *et al.*, 2021), using Lorentz transmission electron microscopy (LTEM). It has been identified that antiskyrmion formation is governed by the competition between uniaxial magnetic anisotropy and dipolar interactions in the presence of the anisotropic DMI. Therefore, antiskyrmions are square-shaped and readily transform into elliptically deformed skyrmions to reduce magnetostatic energy upon changing various parameters (Peng *et al.*, 2020; Karube *et al.*, 2021, 2022).

In $(Fe_{0.63}Ni_{0.30}Pd_{0.07})_3P$, again due to the dominance of uniaxial anisotropy and dipolar interactions, helical and anti-skyrmion spin textures several hundreds of nanometres in size change to micrometre-sized magnetic domain structures as the crystal thickness is increased. Sawtooth-like domain walls and finely branched fractal magnetic domain patterns have been observed near the surface of bulk crystals using magnetic force microscopy (MFM) (Karube *et al.*, 2021). Complex thickness-dependent magnetic textures have also been reported for $Mn_{1.4}PtSn$ (Ma *et al.*, 2020; Sukhanov *et al.*, 2020; Cespedes *et al.*, 2021). MFM studies have provided a clue for understanding the magnetic structure in bulk $(Fe_{0.63}Ni_{0.30}Pd_{0.07})_3P$, which is very different from the LTEM observations of the helical and antiskyrmion spin textures in thin plates. However, the MFM imaging technique probes stray magnetic fields at the sample surface and does not detect the fine magnetic structure deep inside the bulk crystal. In addition, the detailed temperature and field dependence of the fractal magnetic domains was not investigated in the previous MFM study (Karube *et al.*, 2021).

SANS is therefore well suited to the study of fractal magnetic domain structures because it allows quantitative characterization of the thickness-averaged bulk magnetic structure at the mesoscopic length scale, covering the length scales of both fractal magnetic domains and magnetic domain walls (Fig. 1). Small-angle X-ray and neutron scattering are widely used in many fields of science to investigate fractal structures in various systems such as polymers, colloids, porous media *etc.*, since the power-law exponent of the radial intensity profile $I(q) = I_0 q^{-n}$ (Porod slope) directly determines the fractal dimension: mass fractal dimension $D_m = n$ ($1 \leq n \leq 3$) or surface fractal dimension $D_s = 6 - n$ ($3 \leq n \leq 4$), which mathematically quantifies the structural complexity in the system (Schmidt, 1995, 1989; Mildner & Hall, 1986; Martin & Hurd, 1987). The mass fractal describes the density of objects in a given volume, while the surface fractal indicates the roughness of boundary surfaces. For example, $n \simeq 4$ ($D_s \simeq 2$)

in accordance with Porod's law (Porod, 1951) corresponds to smooth surfaces, while $n \simeq 3$ ($D_s \simeq 3$) indicates fractal surfaces finely branched over multiple length scales to fill the three-dimensional space. Kreyssig *et al.* (2009) applied this fractal analysis to highly anisotropic magnetic domain structures in $Nd_2Fe_{14}B$ single crystals using SANS, where the 'surfaces' correspond to the magnetic domain walls. While the original fractal analysis (Schmidt, 1995) was derived assuming isotropic scattering, Kreyssig and co-workers applied this analysis to specific regions between anisotropic scattering, allowing an assumption of isotropic scattering in the selected regions. Sukhanov *et al.* (2020) have reported a similar SANS study and analysis for $Mn_{1.4}PtSn$ single crystals. Nevertheless, to the best of our knowledge, there have been no other examples of fractal magnetic domain structures in single crystals studied by SANS.

In this study, SANS measurements on a bulk single crystal of $(Fe_{0.63}Ni_{0.30}Pd_{0.07})_3P$ were performed, in conjunction with field-dependent magnetometry and MFM imaging. As summarized in Table 1, $(Fe_{0.63}Ni_{0.30}Pd_{0.07})_3P$ has similar magnetic properties to $Nd_2Fe_{14}B$ and $Mn_{1.4}PtSn$ in terms of easy-axis magnetic anisotropy along the tetragonal [001] direction and large saturation magnetizations (demagnetization energy), which can be the sources of fractal magnetic domain textures. In fact, anisotropic SANS patterns similar to those observed in previous studies (Kreyssig *et al.*, 2009; Sukhanov *et al.*, 2020) were observed, and data analysis based on Porod slopes was applied. According to the analysis, we
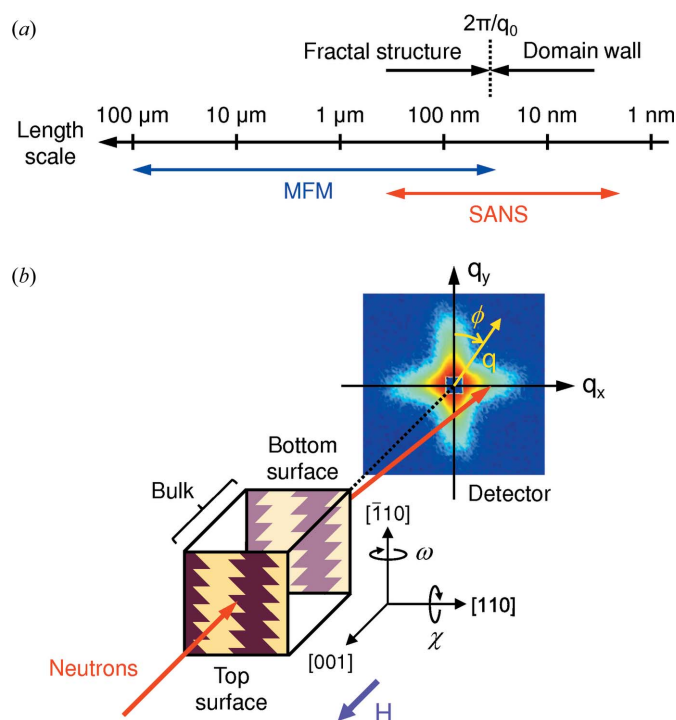

Figure 1
(*a*) The length scales of fractal magnetic domain structure and the domain wall, and the typical length scales accessible by MFM and SANS. (*b*) A schematic diagram of the SANS experiment and a bulk single crystal with sawtooth magnetic domain patterns near (001) surfaces. The rocking angles ω and χ and an azimuthal angle ϕ are also indicated.

Table 1
Magnetic parameters; easy magnetization axis ($T > T_{SR}$), Curie temperature T_C, spin-reorientation temperature T_{SR}, saturation magnetization M_s (at room temperate) and uniaxial magnetic anisotropy constant K_u (at room temperature) for $Nd_2Fe_{14}B$ (Herbst, 1991), $Mn_{1.4}PtSn$ (Vir et al., 2019; Cespedes et al., 2021) and $(Fe_{0.63}Ni_{0.30}Pd_{0.07})_3P$ (Karube et al., 2022).

Material	Space group	Easy axis	T_C (K)	T_{SR} (K)	M_s (kA m^{-1})	K_u (kJ m^{-3})
$Nd_2Fe_{14}B$	$P4_2/mnm$ (D_{4h})	[001]	585	135	1270	4600
$Mn_{1.4}PtSn$	$I\bar{4}2d$ (D_{2d})	[001]	392	170	400	171
$(Fe_{0.63}Ni_{0.30}Pd_{0.07})_3P$	$I\bar{4}$ (S_4)	[001]	398	None	474	28

present evidence for highly anisotropic fractal properties of the magnetic domains in the bulk, and discuss their temperature and magnetic field dependence in detail.

2. Experimental

2.1. Sample preparations

Bulk single crystals of $(Fe_{0.63}Ni_{0.30}Pd_{0.07})_3P$ were synthesized by a self-flux method as detailed in the previous study (Karube et al., 2022). Pure metals and red phosphorus in an off-stoichiometric molar ratio, Fe:Ni:Pd:P = 1.8:1.1:0.6:1.0, were sealed in an evacuated quartz tube. After a preliminary reaction, the sample was cooled slowly from 1243 to 1183 K using a Bridgman furnace. The tetragonal crystal structure with S_4 symmetry (space group $I\bar{4}$) was confirmed by powder X-ray diffraction. The chemical composition of the obtained crystals was determined using energy-dispersive X-ray analysis. The single crystals were cut into rectangles along the (110), ($\bar{1}$10) and (001) planes after the crystal orientations had been checked by X-ray Laue photography.

2.2. Magnetization measurements

Magnetization measurements were carried out using a superconducting quantum interference device magnetometer (MPMS3, Quantum Design). To facilitate comparison with SANS data, the magnetic field in the magnetization curve in Fig. 3(h) was calibrated by multiplying by 1.53, the ratio of the demagnetization factor along the [001] axis of the samples used for the magnetization and SANS measurements.

2.3. MFM measurements

MFM measurements were performed at room temperature using a commercial scanning probe microscope (MFP-3D, Asylum Research) with an MFM cantilever (MFMR, Nano World) at a lift height of 50 nm. A plate-shaped bulk single crystal with a thickness of 0.27 mm was used (supporting information, Fig. S1). The flat (001) surface was prepared by chemical mechanical polishing with colloidal silica. In order to apply external magnetic fields perpendicular to the sample plate, the sample was placed on a cylindrical Nd–Fe–B permanent magnet with a diameter of 3 mm and a thickness of 0.5–3 mm. The magnitude of the field at the surface of the permanent magnet (0.15–0.44 T) was measured using a tesla meter. To facilitate comparison with SANS data, the magnetic fields in Fig. 2 and Fig. S1 were calibrated by multiplying by 0.850, the ratio of the demagnetization factor along the [001] axis of the samples used for the MFM and SANS measurements.

2.4. SANS measurements

SANS measurements were performed using the SANS-I instrument at the Paul Scherrer Institute (PSI), Switzerland. The schematic configuration of the SANS experiment is shown in Fig. 1(b). A bulk single crystal with a thickness of 0.96 mm was installed into a horizontal-field cryomagnet so that both the neutron beam and the field direction were parallel to the [001] axis. The neutron beam with 9 Å wavelength was collimated before the sample, and the scattered neutrons were detected by a two-dimensional detector. We used the following two configurations: (i) a collimator length of 18 m and a detector length of 20 m to cover the low-q region (≥ 0.003 Å^{-1}), and (ii) a collimator length of 8 m and a detector length of 8 m to cover the high-q region (≤ 0.04 Å^{-1}) [$q = (4\pi/\lambda)\sin\theta$, where θ is half the scattering angle and λ is the wavelength of the incident radiation]. For the SANS patterns in Fig. 3, only data collected using the first configuration are presented. For the intensity profiles as a function of q in Figs. 4 and 5 , the data obtained from the two configurations were merged. For all SANS data, background signals from the sample and the instrument were subtracted using the data for the fully polarized ferromagnetic state at 0.8 T. The SANS data before background subtraction in the two configurations are presented in Fig. S3. The field-dependent SANS measurements at 2 and 300 K were performed during a field-increasing process. For each measurement rocking scans were performed, i.e. the cryomagnet was rotated together with the sample around the vertical [$\bar{1}$10] direction (rocking angle ω) and the horizontal [110] direction (rocking angle χ) in the range from −3 to 3° in 0.2° steps. Here, the crystal was precisely aligned so that the origin of the rocking scans ($\omega = \chi = 0°$) corresponds to the configuration with the beam || [001]. The observed FWHM of the rocking curves was ~0.5° for both orientations, as shown in Fig. S4. All the SANS patterns displayed in this paper were obtained by summing over the SANS measurements taken at each angle of the rocking scans (−3 ≤ ω ≤ 3° and −3 ≤ χ ≤ 3°).

3. Results and discussion

3.1. Imaging of fractal magnetic domains by MFM

First, to visualize the fractal magnetic domains in real space, MFM images at room temperature and at several magnetic fields are presented in Fig. 2 at different magnifications. At zero field, complex stripe domains with a main period of about 20 µm, aligned along the [110] and [$\bar{1}$10] axes, are observed [Figs. 2(a)–2(c)]. Smaller subdomains with opposite magnetization are embedded in the stripe domains, and the sawtooth-shaped domain walls are finely branched. As detailed in the

supporting information (Section S2 and Fig. S2), a box-counting analysis (Falconer, 1990; Smith *et al.*, 1996; Han *et al.*, 2002; Lisovskii *et al.*, 2004) of the MFM image reveals that the domain walls exhibit fractal behaviour over the box length scale from 323 to 54 nm, with a fractal dimension of $D = 1.29$ (1). The chirality of the sawtooth pattern is reversed along the two orthogonal axes, which is attributed to the reversed helicity of the Bloch walls deep inside the bulk (Karube *et al.*, 2021). The fast Fourier transform (FFT) of Fig. 2(a) is shown in Fig. 2(d). The large dots aligned horizontally correspond to the period of the main stripe domain and its higher harmonics. As indicated by the yellow ellipses, the intensity distribution of the broad cross-shaped pattern is tilted clockwise from the vertical axis, but anticlockwise from the horizontal axis, reflecting the asymmetric sawtooth domain pattern with $\bar{4}$ symmetry.

At a magnetic field of 0.18 T, the stripe domains are fragmented and transformed into square, letter N- and letter J-shaped domains, as indicated by the red, blue and green circles, respectively [Fig. 2(e)], which are surrounded by a number of smaller self-similar domains with several length scales [Figs. 2(f) and 2(g)]. There is also a $\bar{4}$ symmetry in the square domains themselves and between the N- and J-shaped domains, as in the antiskyrmion spin texture. The FFT pattern

is blurred but still shows the asymmetric cruciform shape [Fig. 2(h)]. Therefore, while the topology of the domains has changed significantly, the anisotropic fractal feature remains.

At a field of 0.25 T, the largest domains become smaller and rounder, and the smallest bubble-like domains exist more sparsely [Figs. 2(i)–2(k)], indicating that both anisotropic and fractal features are suppressed. Correspondingly, the FFT pattern becomes more isotropic [Fig. 2(l)]. Above 0.35 T, the magnetic domain structure disappears and a single domain state is formed (Fig. S1). From the box-counting analysis, the fractal dimensions of the MFM images at 0.18 and 0.25 T were calculated to be 1.23 (1) and 1.22 (1), respectively.

3.2. Characterization of fractal magnetic domains by SANS

Next, we present SANS results obtained at 2 and 300 K and quantitative analyses of the fractal magnetic domain structure, and discuss its magnetic field dependence. The results are considered in comparison with other materials. Finally, we also discuss an additional broad peak structure observed only at 300 K.

3.2.1. SANS patterns and magnetization. Figs. 3(a)–3(f) show SANS patterns at 2 and 300 K at several magnetic fields after background subtraction. At zero field, anisotropic diffuse
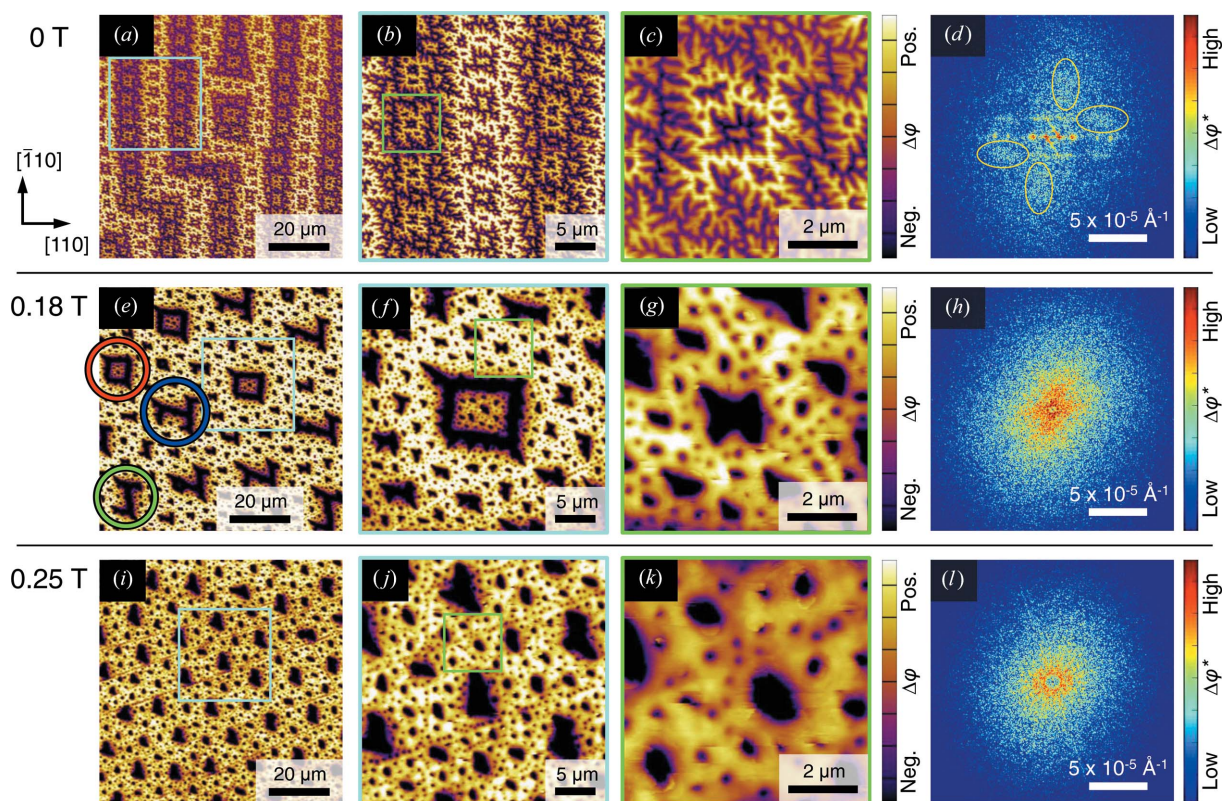

Figure 2
MFM imaging of magnetic domain patterns at the surface of bulk $(Fe_{0.63}Ni_{0.30}Pd_{0.07})_3P$ at room temperature. MFM images at (a)–(c) 0 T, (e)–(g) 0.18 T and (i)–(k) 0.25 T. Panels (b), (f) and (j) show higher-magnification images of the regions outlined in light blue in panels (a), (e) and (i), respectively, and panels (c), (g) and (k) are further magnified images of the regions outlined in light green in panels (b), (f) and (j), respectively. The red, blue and green circles in panel (e) indicate square, letter N- and letter J-shaped domains, respectively. The colour of the MFM images shows the phase shift of the oscillating cantilever ($\Delta\varphi$), corresponding to the stray magnetic fields perpendicular to the sample surface produced by the magnetization. Panels (d), (h) and (l) present the corresponding FFTs of (a), (e) and (i). The yellow ellipses in panel (d) highlight the asymmetric FFT intensity distribution which reflects the sawtooth pattern as governed by the $\bar{4}$ symmetry.

scattering patterns with long tails along the [110] and [$\bar{1}$10] directions are observed at both 2 and 300 K. Note that this anisotropic scattering is present only within the basal plane, with a long correlation length along the easy [001] direction as shown from the rocking scans (Fig. S4). Under external magnetic fields, the anisotropic SANS intensities gradually disappear. The SANS intensities integrated over the region along the [110] and [$\bar{1}$10] directions are plotted against the magnetic field in Fig. 3(g) and compared with magnetization curves in Fig. 3(h). At zero field, the SANS intensity at 2 K is about twice as large as that at 300 K. The SANS intensities at 2 and 300 K decrease smoothly with increasing field and disappear at around 0.5 and 0.3 T, respectively. These critical magnetic fields almost coincide with the saturation fields of the magnetization curve. Therefore, the observed SANS intensities are attributed to scattering from the magnetic domain structures.

Notably, the cross-shaped SANS pattern at zero field is well aligned along the vertical and horizontal directions, except for a slight rotation due to sample misalignment ($\sim$3°), and there is no asymmetric twisting as observed in the FFT of the MFM image. This is because the sawtooth domain pattern reverses for the top and bottom surfaces when viewed from the same direction [Fig. 1(b)] due to the opposite direction of the stray magnetic fields from the two surfaces, as demonstrated in the previous MFM study and micromagnetic simulations (Karube et $al.$, 2021). Thus the asymmetric feature from the sawtooth pattern near the surface becomes smeared in the thickness-averaged magnetic structure probed by SANS. Nevertheless,

as will be shown in the next section, there is an anisotropic fractal character in the SANS pattern.

3.2.2. Fractal analysis at zero field. First, we analyse the SANS data at zero field. The radial SANS intensity profiles $I(q)$ at 2 and 300 K are plotted in Fig. 4 on a log–log scale. Since the SANS pattern is highly anisotropic, $I(q)$ is determined from the azimuthally integrated intensities over narrow regions along the [110] and [$\bar{1}$10] axes ($\mathbf{q} \parallel$ [110]) [Figs. 4(a) and 4(c)] and the regions along the [100] and [010] axes ($\mathbf{q} \parallel$ [100]) [Figs. 4(b) and 4(d)], so that an analysis based on isotropic scattering can be assumed for each direction. At 2 K, $I(q)$ for $\mathbf{q} \parallel$ [110] follows power functions, $I(q) = I_0 q^{-n}$, with two different exponents below and above $q_0 = 0.0138$ Å^{-1}, where the slope changes sharply [Fig. 4(a)]. The power function fitting yields $n = 3.09$ (1) for $q < q_0$ (red line) and $n = 5.54$ (2) for $q > q_0$ (blue line). This characteristic SANS intensity profile is similar to those of $Nd_2Fe_{14}B$ (Kreyssig et $al.$, 2009) and $Mn_{1.4}PtSn$ (Sukhanov et $al.$, 2020), indicating that Porod analysis similar to the previous studies can be applied. The values of n and q_0 for the three different materials at zero field are summarized in Table 2. As discussed in the literature, the power-law behaviour with $n \simeq 3.1$ (surface fractal dimension $D_s \simeq 2.9$) in the low-q region below q_0 shows evidence for a strongly fractal magnetic domain structure. Following convention and assuming a Gaussian distribution, we can estimate the lower limit of length scales over which fractal domain structures exist according to $2\pi/q_0 \simeq 46$ nm. In the high-q region above q_0, scattering from the magnetic domain walls is detected. The exponent $n \simeq 5.5$ obtained
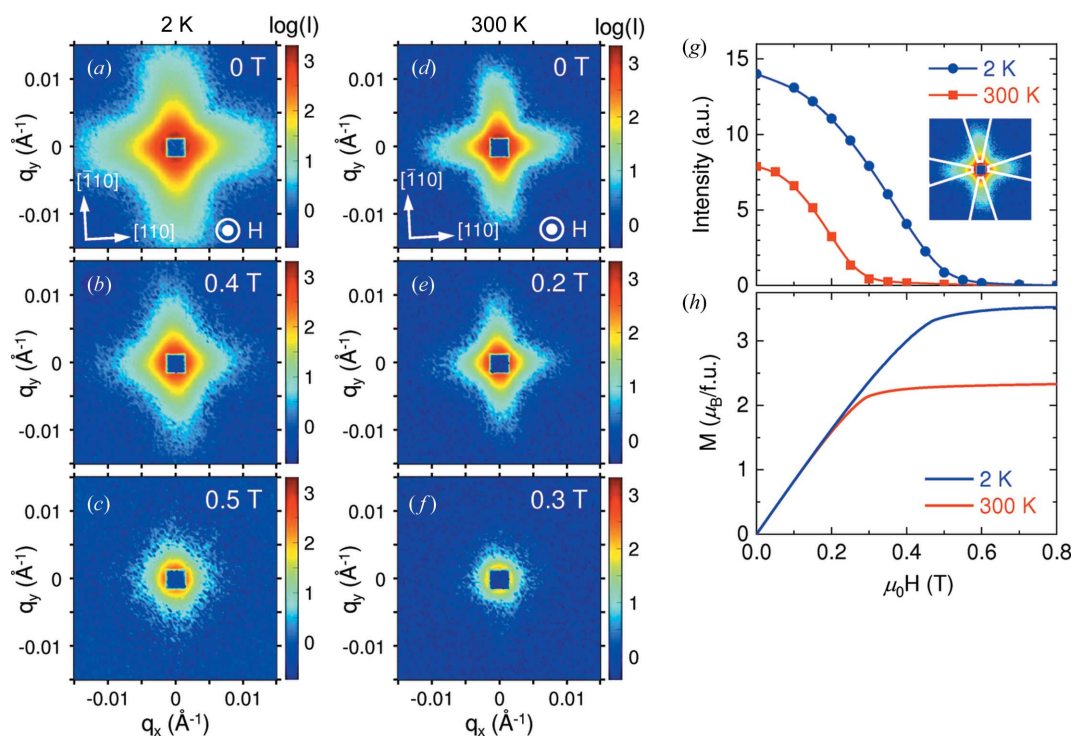

Figure 3
SANS patterns in bulk $(Fe_{0.63}Ni_{0.30}Pd_{0.07})_3P$ at (a)–(c) 2 K and (d)–(f) 300 K at selected magnetic fields. In these SANS images, the non-magnetic scattering from the background was subtracted using the data in the fully polarized state at 0.8 T (Fig. S3). (g), (h) Magnetic field dependence of (g) the integrated SANS intensity and (h) magnetization M at 2 and 300 K. The SANS intensities are integrated over the regions along the [110] and [$\bar{1}$10] directions [white sectors in the inset of panel (g)].

Table 2
Power exponent n and crossover wavevector q_0 at zero field obtained from SANS measurements in $Nd_2Fe_{14}B$ (Kreyssig *et al.*, 2009), $Mn_{1.4}PtSn$ (Sukhanov *et al.*, 2020) and $(Fe_{0.63}Ni_{0.30}Pd_{0.07})_3P$ (this study).

Material	T (K)	n ($q < q_0$)	n ($q > q_0$)	q_0 (Å^{-1})
$Nd_2Fe_{14}B$	200	3.09 (5)	4.84 (6)	0.018
	20	3.73 (3)	–	–
$Mn_{1.4}PtSn$	250	2.65	5.8	0.013
	90	3.65	–	–
$(Fe_{0.63}Ni_{0.30}Pd_{0.07})_3P$	300	3.10 (2)	5.4 (1)	0.0101
	2	3.09 (1)	5.54 (2)	0.0138

above q_0 is much larger than 4, indicating a broad profile at the boundary (Schmidt, 1995; Kreyssig *et al.*, 2009), *i.e.* the magnetization rotates gradually within thick domain walls. On the other hand, $I(q)$ for $\mathbf{q} \parallel [100]$ obeys a single power function without a sharp change in the slope [Fig. 4(b)]. The fitting gives $n = 4.13$ (2) (green line), which is close to Porod's law. Therefore, the fractal feature is present for $\mathbf{q} \parallel [110]$ but not for $\mathbf{q} \parallel [100]$, indicating that the fractality of the magnetic domain structure is highly anisotropic.

At 300 K, compared with the 2 K data, $I(q)$ for $\mathbf{q} \parallel [110]$ shows a similar power-law behaviour with a sharp change in the slope below and above $q_0 = 0.0101$ Å^{-1}, while a weak bump structure is superimposed on the power-law scattering in the higher-q region [indicated with an arrow in Fig. 4(c)]. This high-q bump structure can be seen more clearly under

magnetic fields [Fig. 5(c)]. Power-law fitting over the q region without the bump structure yields $n = 3.10$ (2) for $q < q_0$ (red line) and $n = 5.4$ (1) for $q > q_0$ (blue line), which are almost the same values as the 2 K result. Similarly, $I(q)$ for $\mathbf{q} \parallel [100]$ obeys a single power function in the low-q region, while a clear bump structure is observed in the high-q region as in the case of $\mathbf{q} \parallel [110]$ [Fig. 4(d)]. The power-law fitting gives $n = 4.12$ (6) (green line), which is again very close to the 2 K data. These almost identical exponents to those of the 2 K data in both directions indicate that a similar anisotropic fractal magnetic domain structure is realized at 300 K, with an additional isotropic structure present on even smaller length scales, which will be discussed in detail in Section 3.2.4.

The crossover length $2\pi/q_0$ (~46 nm at 2 K and ~62 nm at 300 K) corresponds to the domain wall width (Kreyssig *et al.*, 2009). Indeed, this value shows good agreement with the domain wall width of antiskyrmions (~52 nm) at room temperature and zero field observed in real-space imaging using the differential phase contrast technique by scanning transmission electron microscopy (Karube *et al.*, 2021). The ratio of $2\pi/q_0$ at 2 K to that at 300 K is 0.73. This difference is explained with the formula for the temperature (T)-dependent domain wall width given by $\delta(T) = \pi[A(T)/K_u(T)]^{1/2}$, where A is the exchange stiffness and K_u is the uniaxial anisotropy constant. Theoretical scaling relations with the saturation magnetization M_s, *i.e.* $A(T) \propto [M_s(T)]^{1.8}$ and $K_u(T) \propto [M_s(T)]^3$, yield $\delta(T) \propto [M_s(T)]^{-0.6}$ (Atxitia *et al.*,
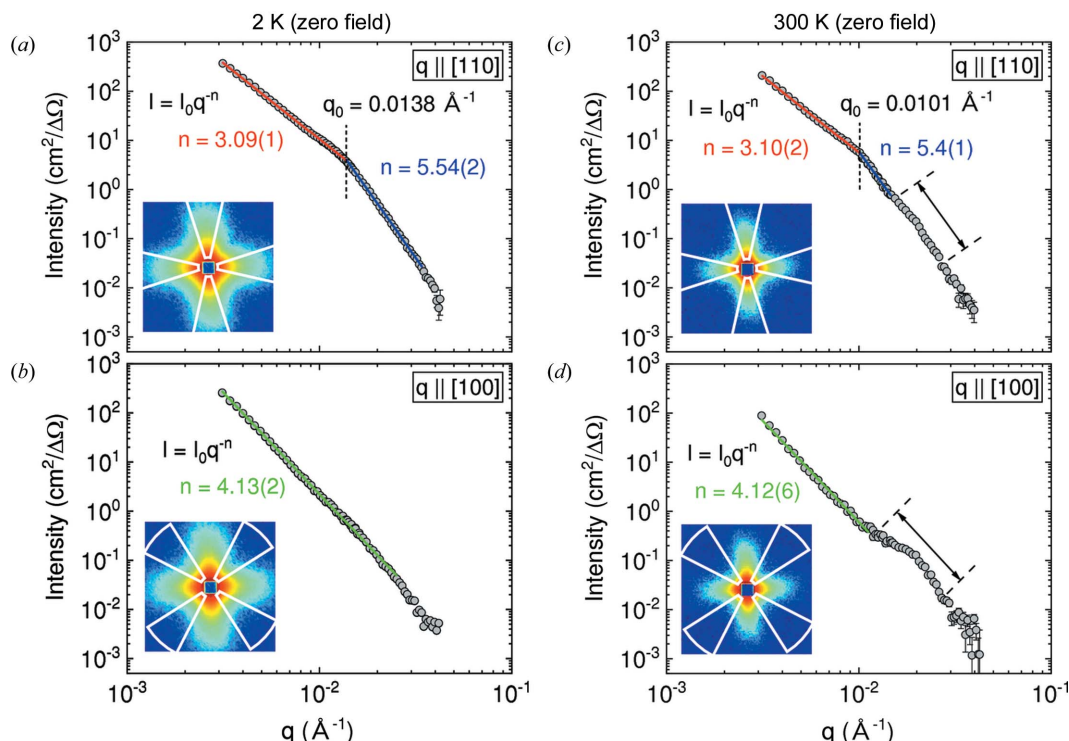

Figure 4
Log–log plots of azimuthally averaged SANS intensity as a function of q at (a), (b) 2 K and (c), (d) 300 K at zero field. SANS intensities are averaged over the regions along (a), (c) the [110] and [$\bar{1}$10] directions (azimuthal angle at $\phi = 357, 87, 177$ and $267°$, with the width of $\Delta\phi = 30°$) and (b), (d) the [100] and [010] axes ($\phi = 42, 132, 222$ and $312°$, $\Delta\phi = 30°$), as indicated by the white sectors in the inset of each panel. The experimental data (grey symbols) are fitted to the power function $I = I_0 q^{-n}$ (solid lines). The crossover momentum q_0 where n changes sharply for $\mathbf{q} \parallel [110]$ is indicated by a vertical dashed line in panels (a) and (c). The range in q of the bump structure observed at 300 K is indicated by an arrow between two dashed lines in panels (c) and (d).

2010; Moreno *et al.*, 2016). Using the saturation magnetizations at 300 and 2 K, the ratio of the domain wall width at 2 K to that at 300 K is calculated to be 0.78, which is in good agreement with the ratio of $2\pi/q_0$ (0.73) determined by SANS.

As shown in Table 2, in $Nd_2Fe_{14}B$ and $Mn_{1.4}PtSn$ the exponent becomes $n \simeq 3.7$ ($D_s \simeq 2.3$), *i.e.* the fractality becomes weaker, below the spin reorientation temperature $T_{SR} = 135$ and 170 K, respectively, where the magnetic moments cant away from the [001] direction (Kreyssig *et al.*, 2009; Sukhanov *et al.*, 2020). In contrast, in $(Fe_{0.63}Ni_{0.30}Pd_{0.07})_3P$, the exponent $n \simeq 3.1$ ($D_s \simeq 2.9$) does not change between 2 and 300 K due to the absence of a temperature-induced spin reorientation in this composition (Karube *et al.*, 2022). These results indicate that easy-axis magnetic anisotropy plays a major role in the formation of fractal magnetic domain structures. The cross-shaped anisotropic SANS pattern is attributed to in-plane magnetocrystalline anisotropy below T_{SR} in $Nd_2Fe_{14}B$ (Pastushenkov *et al.*, 1997; Kreyssig *et al.*, 2009) and to anisotropic DMI in $Mn_{1.4}PtSn$ and $(Fe_{0.63}Ni_{0.30}Pd_{0.07})_3P$, which fix the principal domain walls perpendicular to specific in-plane directions.

While it is difficult to describe precisely the three-dimensional real-space structure of magnetic domains with a fractal dimension close to 3, the finely branched domain structure on the surface of the sample, as observed by MFM, presumably penetrates into the bulk to some extent and forms numerous dagger-like domains from the surface to the inner regions, as has long been discussed in the literature (Kaczér & Gemperle, 1960; Hubert & Schäfer, 1998).

3.2.3. Magnetic field dependence of fractality. Next, the above fractal analysis is extended to data under magnetic fields. The $I(q)$ profiles at various magnetic fields for $\mathbf{q} \parallel [110]$ and $\mathbf{q} \parallel [100]$ at 2 and 300 K are plotted in Fig. 5 on a log–log scale. At 2 K, for $\mathbf{q} \parallel [110]$, as the magnetic field is increased the two different slopes of $I(q)$ below and above q_0 become closer while the scattering intensity decreases [Fig. 5(*a*)]. Note that the kink position at q_0 is independent of the field, as indicated by the vertical dashed line. On the other hand, the single slope of $I(q)$ for $\mathbf{q} \parallel [100]$ is almost constant with respect to the magnetic field [Fig. 5(*b*)].

At 300 K, for $\mathbf{q} \parallel [110]$, a similar field dependence is observed in the low-q region, while the two slopes merge at high fields, except for the presence of the bump structure in the high-q region [Fig. 5(*c*)]. The bump structure becomes clearer as the strong scattering intensity from the power-law component is suppressed by the field. For $\mathbf{q} \parallel [100]$, the slope of $I(q)$ becomes slightly gentler under the field while the high-q bump structure hardly changes [Fig. 5(*d*)].

The exponents n obtained from the power-function fitting at 2 and 300 K are plotted against magnetic field in Fig. 6. Here, n in the low-q region below q_0 for $\mathbf{q} \parallel [110]$ is denoted as $n_{[110]-L}$ (red filled circles), n in the high-q region above q_0 for $\mathbf{q} \parallel [110]$ as $n_{[110]-H}$ (blue filled squares) and n for $\mathbf{q} \parallel [100]$ as $n_{[100]}$ (green open triangles). At 2 K, $n_{[110]-L}$ gradually increases from 3.1 and $n_{[110]-H}$ gradually decreases from 5.5, both approaching 4 as the field is increased up to the saturation field around 0.5 T [Fig. 6(*a*)]. On the other hand, $n_{[100]}$ always stays around 4 in the whole field region up 0.5 T. This magnetic
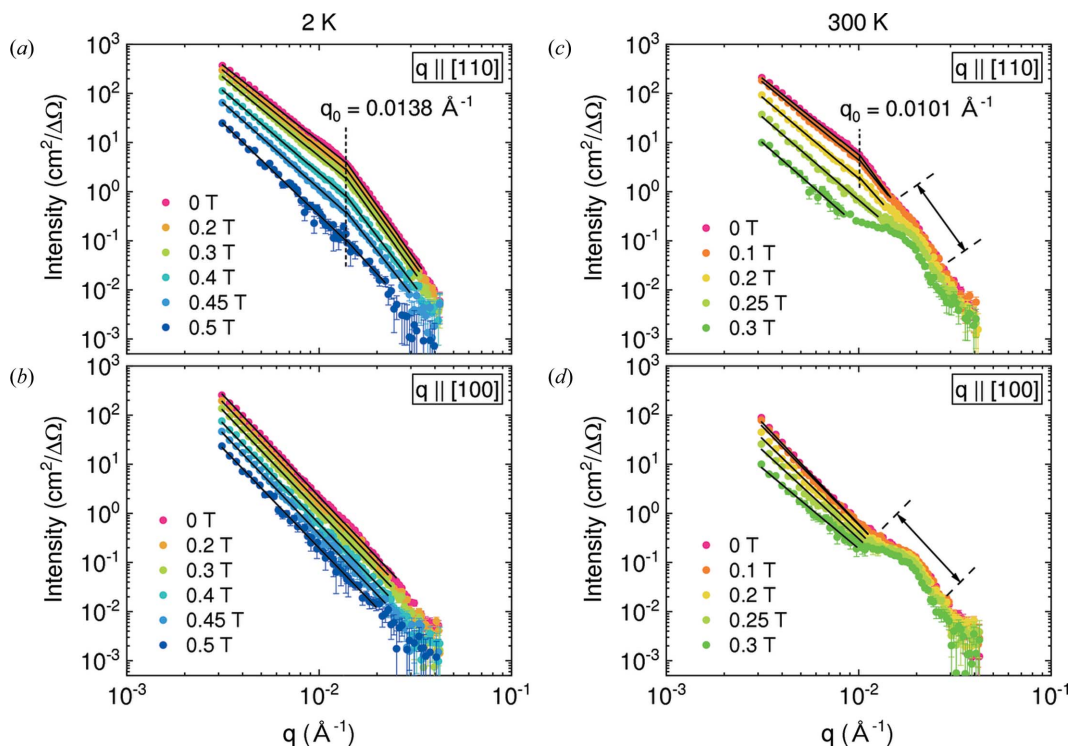

Figure 5
Log–log plots of azimuthally averaged SANS intensity as a function of q at (*a*), (*b*) 2 K and (*c*), (*d*) 300 K at various magnetic fields. SANS intensities are averaged over the regions along (*a*), (*c*) the [110] and [$\bar{1}$10] directions and (*b*), (*d*) the [100] and [010] directions, as defined in Fig. 4. The experimental data (closed symbols) are fitted to the power function (black solid lines). The crossover momentum q_0 for $\mathbf{q} \parallel [110]$ is indicated by a vertical dashed line in panels (*a*) and (*c*). The range in q of the bump structure observed at 300 K is indicated by an arrow between two dashed lines in panels (*c*) and (*d*).
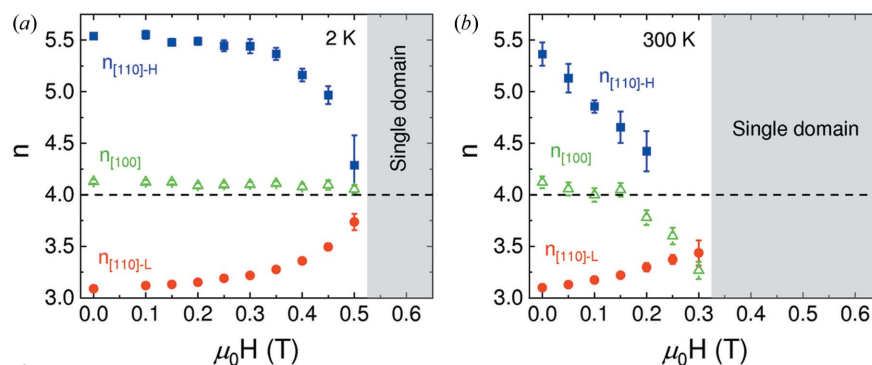
Figure 6
Magnetic field dependence of the power-law exponent n at (a) 2 K and (b) 300 K. The value of n in the region of $q < q_0$ ($q > q_0$) for **q** ∥ [110] is defined as $n_{[110]\text{-L}}$ ($n_{[110]\text{-H}}$) and shown by red (blue) filled symbols, while n for **q** ∥ [100] is defined as $n_{[100]}$ and indicated with green open symbols. The field region of the single-domain state is indicated with grey shading.

field dependence at 2 K indicates a gradual suppression of fractality of the magnetic domain structure by the field while maintaining the anisotropy.

At 300 K, $n_{[110]\text{-L}}$ increases from 3.1 to 3.4 and $n_{[110]\text{-H}}$ decreases with increasing magnetic field to the saturation field around 0.3 T [Fig. 6(b)]. Above 0.25 T, the two power functions merge and $n_{[110]\text{-H}}$ is not well defined. In contrast to the 2 K data, $n_{[100]}$ remains around 4 at low fields but starts to decrease above 0.2 T, reaching almost the same value as $n_{[110]\text{-L}}$. These plots at 300 K clearly show a field-induced change from anisotropic strong fractal to isotropic weak

fractal. This field dependence is qualitatively consistent with the MFM results, where the fractal domain pattern becomes isotropic above 0.2 T [Figs. 2(i)–2(k)].

3.2.4. Broad peak structure. Finally, we analyse the high-q bump structure observed only at 300 K [Figs. 5(c) and 5(d)] and consider its possible origin in Fig. 7. As shown in Figs. 7(a) and 7(b), for each of **q** ∥ [110] and **q** ∥ [100] the broad peak component was extracted by subtracting the power-law contribution from $I(q)$ and then fitted to a Gaussian function. In both directions, the broad peak is robust against magnetic field and observed up to 0.4 T, while its centre shifts to lower q above 0.3 T, which is near the boundary between the multi-domain and single-domain states.

These results suggest that the broad SANS peak can be ascribed to an isotropic spatial distribution of inhomogeneously magnetized regions, whose magnitude is distinct from those in the matrix domains, as depicted schematically in Fig. 7(c). Similar arguments have been reported for Fe–Ga alloys (Laver *et al.*, 2010; Gou *et al.*, 2021). The average spacing of the magnetic inhomogeneities, defined as $\xi = 2\pi/q_G$ (here, q_G is the centre of the Gaussian peak), is plotted against field in Fig. 7(d). In both directions, $\xi \simeq 40$ nm is almost independent of the field and starts to increase above 0.3 T.
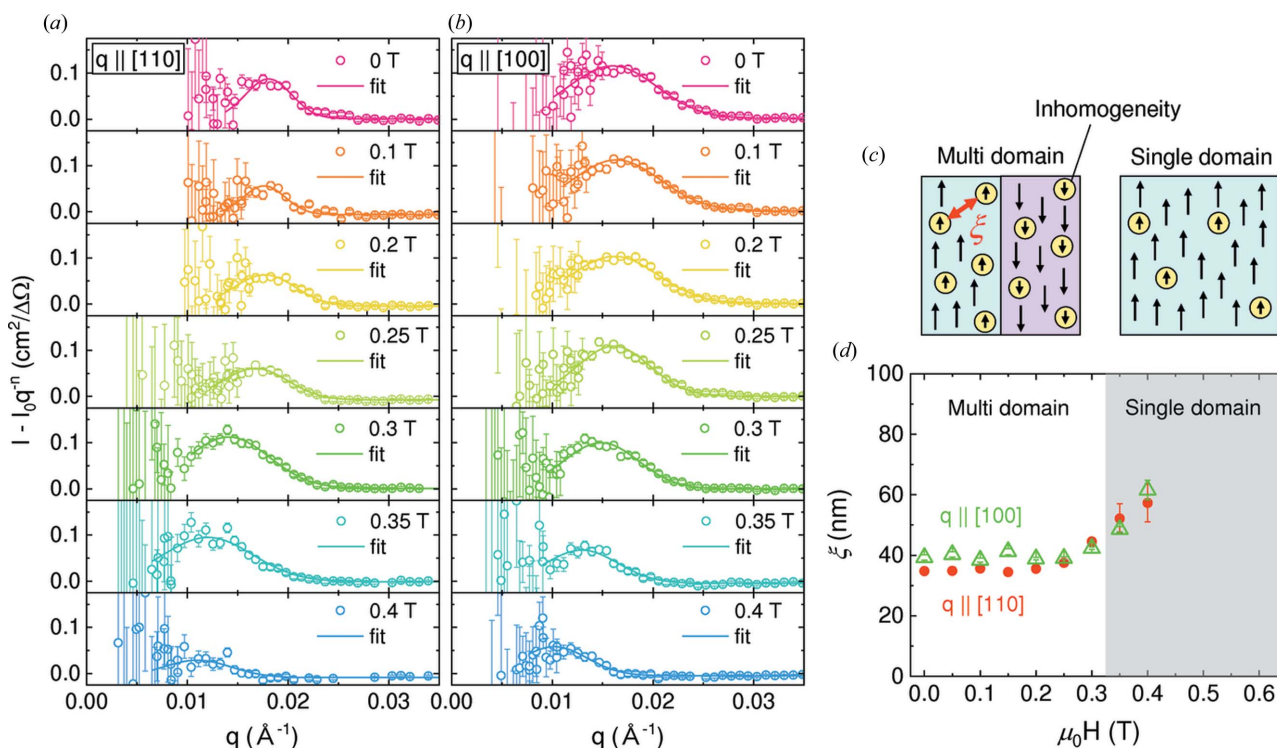

Figure 7
Analysis of the broad SANS peak at 300 K. (a), (b) Residual SANS intensity after subtraction of the power-law component at 300 K and various magnetic fields for (a) **q** ∥ [110] and (b) **q** ∥ [100]. The experimental data (open symbols) are fitted to a Gaussian function (solid line). (c) Schematic figures of proposed field-dependent magnetic inhomogeneities (yellow regions) within the matrix magnetic domains (light-blue and purple regions). (d) Magnetic field dependence of the average spacing ξ (= $2\pi/q_G$) of the magnetic inhomogeneities for **q** ∥ [110] (red symbols) and **q** ∥ [100] (green symbols), where q_G is the peak centre of the Gaussian fitting. The grey shading represents the field-induced single-domain region.

The robustness of the broad peak against the field can be well explained by the fact that the magnetization process at low fields is governed by the displacement of domain walls. Once the single-domain state is attained and the field is further increased, some of the inhomogeneous magnetizations are forced to order and those that remain are sparse. The disappearance of the broad peak at 2 K may be accounted for by the uniform magnetization when the ferromagnetic ordering is fully developed at low temperatures. Further studies from both high-resolution real-space and reciprocal-space experiments at various temperatures are needed to characterize this disordered magnetic state in more detail.

4. Conclusions

We have investigated the fractal magnetic domain structure in bulk single crystals of $(Fe_{0.63}Ni_{0.30}Pd_{0.07})_3P$, a unique anti-skyrmion material with S_4 symmetry, using SANS and MFM. The SANS intensity profile shows a power-law behaviour with an exponent close to 3, demonstrating the existence of a fractal magnetic domain structure in the bulk on length scales down to the domain wall width where the slope of the intensity profile changes. The fractal domain structure at zero field is highly anisotropic, with the scattering intensity existing mainly along the [110] and [$\bar{1}$10] directions, and gradually disappears with increasing magnetic field. At 2 K, the anisotropic feature remains until the fractal domain structure completely disappears at high fields, whereas at 300 K the anisotropic fractal structure changes to an isotropic fractal one as the magnetic field is increased. Furthermore, the SANS profile shows an additional broad peak only at 300 K, which is isotropic and robust against magnetic fields, suggesting inhomogeneous magnetizations within the domains.

The present study provides a quantitative understanding of the anisotropic fractal magnetic domain structure on various length scales in bulk $(Fe_{0.63}Ni_{0.30}Pd_{0.07})_3P$, and demonstrates the prominent capability of SANS for studying fractal structures in magnetic systems.

References

Atxitia, U., Hinzke, D., Chubykalo-Fesenko, O., Nowak, U., Kachkachi, H., Mryasov, O. N., Evans, R. F. & Chantrell, R. W. (2010). *Phys. Rev. B*, **82**, 134440.

Bogdanov, A. N. & Yablonskii, D. A. (1989). *Sov. Phys. JETP*, **68**, 101–103.

Falconer, K. (1990). *Fractal Geometry: Mathematical Foundations and Applications.* Chichester: Wiley.

Gou, J., Ma, T., Liu, X., Zhang, C., Sun, L., Sun, G., Xia, W. & Ren, X. (2021). *NPG Asia Mater.* **13**, 6.

Han, B.-S., Li, D., Zheng, D.-J. & Zhou, Y. (2002). *Phys. Rev. B*, **66**, 014433.

Herbst, J. F. (1991). *Rev. Mod. Phys.* **63**, 819–898.

Hubert, A. & Schäfer, R. (1998). *Magnetic Domains: The Analysis of Magnetic Microstructures.* Berlin: Springer.

Kaczér, J. & Gemperle, R. (1960). *Czech. J. Phys.* **10**, 505–510.

Karube, K., Peng, L. C., Masell, J., Hemmida, M., Krug von Nidda, H.-A., Kézsmárki, I., Yu, X. Z., Tokura, Y. & Taguchi, Y. (2022). *Adv. Mater.* **34**, 2108770.

Karube, K., Peng, L. C., Masell, J., Yu, X. Z., Kagawa, F., Tokura, Y. & Taguchi, Y. (2021). *Nat. Mater.* **20**, 335–340.

Kreyssig, A., Prozorov, R., Dewhurst, C. D., Canfield, P. C., McCallum, R. W. & Goldman, A. I. (2009). *Phys. Rev. Lett.* **102**, 047204.

Laver, M., Mudivarthi, C., Cullen, J. R., Flatau, A. B., Chen, W.-C., Watson, S. M. & Wuttig, M. (2010). *Phys. Rev. Lett.* **105**, 027202.

Leonov, A. O., Monchesky, T. L., Romming, N., Kubetzka, A., Bogdanov, A. N. & Wiesendanger, R. (2016). *New J. Phys.* **18**, 065003.

Lisovskii, F. V., Lukashenko, L. I. & Mansvetova, E. G. (2004). *JETP Lett.* **79**, 352–354.

Ma, T., Sharma, A. K., Saha, R., Srivastava, A. K., Werner, P., Vir, P., Kumar, V., Felser, C. & Parkin, S. S. P. (2020). *Adv. Mater.* **32**, 2002043.

Malozemoff, A. P. & Slonczewski, J. C. (1979). *Magnetic Domain Walls in Bubble Materials.* New York: Academic Press.

Martin, J. E. & Hurd, A. J. (1987). *J. Appl. Cryst.* **20**, 61–78.

Mildner, D. F. R. & Hall, P. L. (1986). *J. Phys. D Appl. Phys.* **19**, 1535–1545.

Moreno, R., Evans, R. F. L., Khmelevskyi, S., Muñoz, M. C., Chantrell, R. W. & Chubykalo-Fesenko, O. (2016). *Phys. Rev. B*, **94**, 104433.

Mühlbauer, S., Binz, B., Jonietz, F., Pfleiderer, C., Rosch, A., Neubauer, A., Georgii, R. & Böni, P. (2009). *Science*, **323**, 915–919.

Mühlbauer, S., Honecker, D., Périgo, A., Bergner, F., Disch, S., Heinemann, A., Erokhin, S., Berkov, D., Leighton, C., Eskildsen, M. R. & Michels, A. (2019). *Rev. Mod. Phys.* **91**, 015004.

Nagaosa, N. & Tokura, Y. (2013). *Nature Nanotech.* **8**, 899–911.

Nayak, A. K., Kumar, V., Ma, T., Werner, P., Pippel, E., Sahoo, R., Damay, F., Rößler, U. K., Felser, C. & Parkin, S. S. P. (2017). *Nature*, **548**, 561–566.

Pastushenkov, Y. G., Forkl, A. & Kronmüller, H. (1997). *J. Magn. Magn. Mater.* **174**, 278–288.

Peng, L. C., Takagi, R., Koshibae, W., Shibata, K., Nakajima, K., Arima, T., Nagaosa, N., Seki, S., Yu, X. Z. & Tokura, Y. (2020). *Nat. Nanotechnol.* **15**, 181–186.

Porod, G. (1951). *Kolloid-Z.* **124**, 83–114.

Schmidt, P. W. (1989). *The Fractal Approach to Heterogeneous Chemistry: Surfaces, Colloids, Polymers*, edited by D. Avnir, pp. 67–79. Chichester: Wiley.

Schmidt, P. W. (1995). *Modern Aspects of Small-Angle Scattering*, edited by H. Brumberger, pp. 1–56. Dordrecht: Kluwer Academic.

Smith, T. G., Lange, G. D. & Marks, W. B. (1996). *J. Neurosci. Methods*, **69**, 123–136.

Sukhanov, A. S., Cespedes, B. E. Z., Vir, P., Cameron, A. S., Heinemann, A., Martin, N., Chaboussant, G., Kumar, V., Milde, P., Eng, L. M., Felser, C. & Inosov, D. S. (2020). *Phys. Rev. B*, **102**, 174447.

Tokura, Y. & Kanazawa, N. (2021). *Chem. Rev.* **121**, 2857–2897.

Vir, P., Kumar, N., Borrmann, H., Jamijansuren, B., Kreiner, G., Shekhar, C. & Felser, C. (2019). *Chem. Mater.* **31**, 5876–5880.

Yu, X. Z., Onose, Y., Kanazawa, N., Park, J. H., Han, J. H., Matsui, Y., Nagaosa, N. & Tokura, Y. (2010). *Nature*, **465**, 901–904.

Zuniga Cespedes, B. E., Vir, P., Milde, P., Felser, C. & Eng, L. M. (2021). *Phys. Rev. B*, **103**, 184411.